Physics of Plasmas

Benchmarking and validation of global model code for negative hydrogen ion sources

Cite as: Phys. Plasmas **25**, 113509 (2018); https://doi.org/10.1063/1.5050029
Submitted: 26 July 2018 . Accepted: 25 October 2018 . Published Online: 14 November 2018

Wei Yang, Sergey N. Averkin, Alexander V. Khrabrov, Igor D. Kaganovich, You-Nian Wang, Spyridon Aleiferis, and Panagiotis Svarnas

Benchmarking and validation of global model code for negative hydrogen ion sources

Wei Yang,[1,2] Sergey N. Averkin,[3,4,5] Alexander V. Khrabrov,[2] Igor D. Kaganovich,[2,a)] You-Nian Wang,[1,b)] Spyridon Aleiferis,[6,c)] and Panagiotis Svarnas[6]
[1]*Key Laboratory of Materials Modification by Laser, Ion, and Electron Beams (Ministry of Education), School of Physics, Dalian University of Technology, Dalian 116024, China*
[2]*Princeton Plasma Physics Laboratory, Princeton University, Princeton, New Jersey 08543, USA*
[3]*Tech-X Corporation, Boulder, Colorado 80303, USA*
[4]*Center for Integrated Plasma Studies, University of Colorado, Boulder, Colorado 80305, USA*
[5]*Aerospace Engineering Program, Worcester Polytechnic Institute, Worcester, Massachusetts 01609, USA*
[6]*High Voltage Laboratory, Electrical and Computer Engineering Department, University of Patras, Rion-Patras 26504, Greece*

(Received 26 July 2018; accepted 25 October 2018; published online 14 November 2018)

Benchmarking and validation are prerequisites for using simulation codes as predictive tools. In this work, we have developed a Global Model for Negative Hydrogen Ion Source (GMNHIS) and performed benchmarking of the GMNHIS against another independently developed code, Global Enhanced Vibrational Kinetic Model (GEVKM). This is the first study to present a quite comprehensive benchmarking test of this kind for models of negative hydrogen ion sources (NHIS), and excellent agreements have been achieved for collisional energy loss per electron-ion pair created, electron number density, electron temperature, densities of H_3^+ and H_2^+ ions, and densities of H(n = 1–3) atoms. Very small discrepancies in number densities of H^- ions and H^+ ions, as well as the vibrational distribution function of hydrogen molecules, can be attributed to the differences in the chemical reactions datasets. The GEVKM includes additional chemical reactions that are more important at high pressures. In addition, we validated the GMNHIS against experimental data obtained in an electron cyclotron resonance discharge used for H^- production. The model qualitatively (and even quantitatively for certain conditions) reproduces the experimental H^- number density. The H^- number density as a function of pressure first increases at pressures below 1.6 Pa and then saturates for higher pressures. This dependence was analyzed by evaluating contributions from different reaction pathways to the creation and loss of the H^- ions. The developed codes can be used for predicting the H^- production, improving the performance of NHIS, and ultimately optimizing the parameters of negative ion beams for fusion reactors. *Published by AIP Publishing.* https://doi.org/10.1063/1.5050029

I. INTRODUCTION

Negative Hydrogen Ion Sources (NHIS) are used for the production of energetic beams of neutral hydrogen atoms for plasma heating and plasma current drive in magnetic fusion devices, where a beam of 1 MeV energy level is required to sustain the plasma in the steady state.[1] The neutralization efficiency of negative hydrogen ions remains acceptable (∼60%) for such or even higher kinetic energy and is almost independent of the beam energy above 100 keV/nucleon. On the other hand, for positive ions, the neutralization efficiency rapidly decreases as the beam energy exceeds 60 keV/nucleon and becomes negligible in the MeV energy range.[2] Negative ions, instead of positive ions, are to be utilized for ITER and future fusion reactors because of their high neutralization efficiency at high energies required.

The production mechanisms in NHIS are classified into two types: surface production and volume production. In a surface source, energetic H atoms and positive ions are converted into H^- ions on surfaces covered with a low-work-function material as they collide with the surface plasma source electrodes.[3] Deposition of a material with a low work function (typically cesium) on the electrode is required to enhance the negative hydrogen ion production.[4] Although the use of cesium allows negative ion sources to meet the specifications required for ITER,[5] it may cause problems in maintenance and also unstable source operation.[1] The above difficulties can be avoided with an ion source operating without cesium, which is based on a volume process of the H^- ion production. In such a process, the H^- ions are formed directly in the plasma volume through the following two-step process:[6]

$$H_2(v) + e(\varepsilon > 12\text{eV}) \rightarrow H_2(v') + e + h\nu(\text{EV}), \quad (1)$$

$$H_2(v) + e\,(\varepsilon < 2\text{eV}) \rightarrow H^- + H(\text{DA}). \quad (2)$$

In the first step, vibrationally excited hydrogen molecules are produced mainly in collisions with fast electrons through

[a)]E-mail: ikaganov@pppl.gov
[b)]E-mail: ynwang@dlut.edu.cn
[c)]Current addresses: EUROfusion Consortium, JET, Culham Science Centre, Abington OX14 3DB, United Kingdom and Fusion Technology Group, National Centre for Scientific Research 'Demokritos,' 15310 Agia Paraskevi, Athens, Greece.

excitation (EV), which refers to excitation to singlet states followed by radiative decay. In the second step, electrons attach to vibrationally excited hydrogen molecules in the process of dissociative attachment (DA) to form negative hydrogen ions. It was theoretically[7] and experimentally[6] proven that vibrationally excited hydrogen molecules have a significantly higher cross section for the DA reaction. Because the DA reaction makes a major contribution to the volume production of negative ions, it was extensively reported in the past.[8–10] The cross section of the DA process is strongly dependent on both the electron energy and the initial vibrational state.[7] The vibrational kinetics is governed by excitation and deactivation of vibrational levels and is characterized by the vibrational distribution function (VDF). The VDF depends on the operational parameters and design of the ion source.

To improve the performance of the volume-production NHIS, it is important to understand the mechanisms of the volume production of H^- ions and related plasma physics. Most importantly, one needs to identify the plasma conditions for enhanced production of cold electrons for DA and hot electrons for EV processes, which requires sophisticated diagnostics and detailed characterization of the ion source. In traditional volume-production sources, the plasma is produced in hot-filament arcs.[11] However, there is a tendency to introduce radio-frequency (RF)[1,4,12–19] or electron cyclotron resonance (ECR)[20–23] sources. Arc sources suffer from limited lifetime of the filaments, and the evaporated material may contaminate the plasma.[24] In contrast to short-lived filament sources, RF and ECR sources allow for continuous operation, which is necessary for ITER and prospective fusion reactors. Consequently, RF and ECR–based NHIS have been widely studied by many researchers. RF plasma sources have been developed and well experienced in Garching (Max Plank Institute of Plasma Physics, IPP),[1,4,12–14] Padova,[15–18] and Japan[19] in the last few years. A very low pressure of 0.3 Pa is required inside the NHIS to guarantee the survivability of H^- ions.[12] The plasma generated in the driver chamber enters the expansion region where a magnetic filter is added at the source periphery.[12] The magnetic field is necessary to keep hot electrons ($T_e > 2$ eV) away from the regions where the H^- ions are generated, in order to avoid collisional destruction of the negative ions. Several NHIS designs have been proposed. Recently, Averkin *et al*. proposed a high current negative hydrogen ion source (HCNHIS).[25,26] The HCNHIS consists of a high-pressure RF discharge chamber where high vibrational states of molecular hydrogen are mainly generated. The plasma and gas flow in the discharge chamber is controlled (reduced) by a series of bypass tubes and enters through a nozzle into a low-pressure negative hydrogen ion production chamber, where H^- ions are produced mainly by the DA process. Aleiferis *et al*. studied the effect of the balance between vibrational excitation and ionization on negative hydrogen ion production in an ECR volume source.[23]

In the past few decades, numerical simulations have become a valuable tool for improving the understanding of discharge physics and can provide theoretical predictions, especially in cases where diagnostic measurements are expensive or difficult to achieve in an experimental setup. Global models have been developed by many researchers to study hydrogen discharges.[27–32] A verified and validated model is required to characterize the mechanism of volume production of H^- ions and to further improve the NHIS performance. Here, by verification we mean a comparison between simulation results and analytical solution, while validation is a comparison with experimental data.[33] However, analytical solutions are available only in a limited number of cases and chemically reacting plasmas in NHIS are not one of them. Therefore, comparison of different codes with each other (benchmarking) and comparison of simulation results with experimental data (validation) are both important for achieving the goal of making codes usable as predictive tools.[34–36] In this paper, we perform both benchmarking and validation. First, we present benchmarking of the Global Model for Negative Hydrogen Ion Source (GMNHIS), which was developed based on the previous study[28] against the Global Enhanced Vibrational Kinetic Model (GEVKM).[25,26] The chamber used in the models is based on the RF source developed by Gao *et al*.,[37,38] but with only the driver region considered. Gao *et al*.[37,38] focused mainly on characterizing the electron properties, while in this study we focus on the H^- ion production in the NHIS. Subsequently, we validate the GMNHIS against experimental measurements in an ECR discharge, where the data on negative ion production under different discharge conditions are available.[23] The plasma in the experimental reactor is sustained by a 2D network of five dipolar ECR plasma sources.[23] The negative ion production is predicted using the GMNHIS with an experimentally measured electron energy distribution function (EEDF).[23]

This paper is organized as follows: The simulation model, i.e., GMNHIS, subject to benchmarking and validation is described in Sec. II, followed by a detailed description of the plasma chemistry reaction set for H_2. The benchmarking results for RF discharge obtained with the two global-model codes, GMNHIS and GEVKM, are given in Sec. III. A comparison between GMNHIS simulation results and experimental measurements in an ECR discharge is provided in Sec. IV. The conclusions are given in Sec. V.

II. MODEL DESCRIPTION

A global model is also called a zero-dimensional model because it does not solve numerically for the spatial variation of plasma properties but rather relies upon an analytical solution for the respective profiles. The power is assumed to be deposited uniformly into the plasma bulk. A Maxwellian EEDF is assumed in the GMNHIS, but the code can be modified to account for a non-Maxwellian EEDF.[32,39–42] Ions are at the same temperature as the neutral gas and this temperature is fixed in the simulation at 600 K (although modification can be easily introduced to account for gas heating). Four fundamental conservation laws are used in the formulation of the GMNHIS: mass conservation described via a particle balance for each species except for the H_2 molecules; charge conservation, reduced to the quasi-neutrality condition, the H_2 density determined by the equation of state for total particle number density, and energy conservation law expressed through power balance. The resulting balance

conditions present a system of 24 coupled nonlinear ordinary differential equations which are numerically solved. The benchmarking and validation are performed for a cylindrical RF source[37,38] with a reactor radius R and height L and for a cube-shaped ECR matrix source, respectively.[23]

A. Particle balance

The particle balance for neutral species other than H_2 molecules is given as[43]

$$n_i u_{B,i} \frac{A_{\text{eff}1,i}}{V} - \Gamma_j \frac{A_n}{V} + \sum R_j = 0. \tag{3}$$

The first term shows that ions reaching the walls are recycled inside the plasma as neutrals, where n_i is the volume-averaged number density of ions, and V is the volume of the discharge chamber; $V = \pi R^2 L$ for a cylindrical chamber and $V = XYZ$ for a rectangular parallelepiped chamber with side lengths X, Y, and Z. For a cube, three side lengths are equal and $V = L^3$. Next, $u_{B,i} = (eT_e/m_i)^{1/2}[(1+\alpha_s)/(1+\alpha_s\gamma)]^{1/2}$ is the Bohm speed of positive ions modified due to the presence of H^-,[44,45] where e is the elementary charge, T_e is the electron temperature measured in eV, m_i is the ion mass, and $\gamma = T_e/T_-$, T_- being the temperature of the negative ions. The electronegativity at the sheath edge α_s is determined based on the work of Thorsteinsson and Gudmundsson.[45] The effective areas are given for the two chamber shapes, respectively, as[43,46]

$$A_{\text{eff}1,i} = (2-\beta)\pi R^2 h_{L,i}/\Lambda_{L,i} + 2\pi R L h_{R,i}/\Lambda_{R,i}, \tag{4}$$

$$A_{\text{eff}1,i} = (2-\beta)XY h_{z,i}/\Lambda_{z,i} + 2YZ h_{x,i}/\Lambda_{x,i} + 2XZ h_{y,i}/\Lambda_{y,i}, \tag{5}$$

where $\beta = 1$ corresponds to a perfect open boundary at the bottom of the source chamber. In that case, the ions flowing out of the bottom of the source chamber do not recycle as neutrals. The value $\beta = 0$ corresponds to a closed boundary. The quantity h_i represents edge-to-center density ratio for the positive ion species numbered i. For a cylindrical chamber, it is given as[47]

$$h_{R,i} = 0.80\left(4 + \frac{\eta R}{\lambda_i} + \left(\frac{0.80 R u_{B,i}}{\chi_{01} J_1(\chi_{01}) D_{a,i}}\right)^2\right)^{-1/2} \Big/ (1+\alpha_0), \tag{6}$$

$$h_{L,i} = 0.86\left(3 + \frac{\eta L}{2\lambda_i} + \left(\frac{0.86 L u_{B,i}}{\pi D_{a,i}}\right)^2\right)^{-1/2} \Big/ (1+\alpha_0). \tag{7}$$

For a rectangular parallelepiped (box) chamber, it is given as

$$h_{L_{edge},i} = 0.86\left(3 + \frac{\eta L_{edge}}{2\lambda_i} + \left(\frac{0.86 L_{edge} u_{B,i}}{\pi D_{a,i}}\right)^2\right)^{-1/2} \Big/ (1+\alpha_0), \tag{8}$$

where L_{edge} is X, Y, or Z, $D_{a,i} = D_i(1+\gamma+\gamma\alpha_s)/(1+\gamma\alpha_s)$ is the ambipolar diffusion coefficient with the respective diffusion coefficient D_i for positive ions, and λ_i is the ion mean free path. D_i and λ_i will be further discussed later. $\alpha_0 \approx (3/2)\alpha$ is the central electronegativity,[47] and $\eta = 2T_+/(T_+ + T_-) = 1$ based on the assumptions of equal temperatures of ions and gas. All Λ_i are the ratios of the volume-averaged to center densities. For the cylindrical chamber, they are given as[26]

$$\Lambda_{R,i} = 0.70 b_{R,i}/(1+b_{R,i}) + 2/\chi_{01} J_1(\chi_{01})/(1+b_{R,i}), \tag{9}$$

$$\Lambda_{L,i} = 0.85 b_{L,i}/(1+b_{L,i}) + 2/(\pi + \pi b_{L,i}), \tag{10}$$

where $J_1(\chi)$ is the first-order Bessel function and χ_{01} is the first zero of the zero-order Bessel function $J_0(\chi)$. For a rectangular parallelepiped chamber, Λ_i is given as

$$\Lambda_{L_{edge},i} = 0.85 b_{L_{edge},i}/(1+b_{L_{edge},i}) + 2/(\pi + \pi b_{L_{edge},i}). \tag{11}$$

We have $b_{R,i} = 2(\lambda_i/R)/(T_e/T_{gas})$, $b_{L,i} = 2(\lambda_i/L)/(T_e/T_{gas})$, and $b_{L_{edge},i} = 2(\lambda_i/L_{edge})/(T_e/T_{gas})$,[26] where T_{gas} is the gas temperature.

The second term in Eq. (3) accounts for the neutrals flowing out of the bottom of the chamber if the bottom is not closed, where $A_n = \beta\pi R^2$ for the cylindrical chamber and $A_n = \beta XY$ for a box. $\Gamma_j = n_j v_j/4$ is the thermal flux,[43] where n_j is the number density of neutrals, and the mean velocity of neutral species is $v_j = (8eT_j/\pi m_j)^{1/2}$. m_j and T_j are, respectively, the mass and temperature of the j-th species. The quantity R_j in the third term of Eq. (3) is the reaction rate for the creation/loss process of neutral species j.

The particle balance for the ion species is given as[43]

$$-n_i u_{B,i} \frac{A_{\text{eff},i}}{V} + \sum R_i = 0, \tag{12}$$

where R_i is the volume creation/loss rate for ion species i. The effective areas for ion loss for the two chamber shapes in question are given as

$$A_{\text{eff},i} = 2\pi R^2 h_{L,i}/\Lambda_{L,i} + 2\pi R L h_{R,i}/\Lambda_{R,i}, \tag{13}$$

$$A_{\text{eff},i} = 2XY h_{z,i}/\Lambda_{z,i} + 2YZ h_{x,i}/\Lambda_{x,i} + 2XZ h_{y,i}/\Lambda_{y,i}. \tag{14}$$

The total particle number density is constrained by the given operating pressure P. Moreover, the discharge is assumed to satisfy the quasi-neutrality condition. These two criteria can be expressed, respectively, as

$$P = \sum_j n_j k_B T_{gas}, \tag{15}$$

$$n_e = n_{H_3^+} + n_{H_2^+} + n_{H^+} - n_{H^-}, \tag{16}$$

where k_B is the Boltzmann constant.

B. Power balance

The power balance refers to the balance between the absorption power and the bulk power losses caused by elastic and inelastic collisions, and also power losses due to charged species flowing to the walls

$$P_{abs} = P_V + P_W, \tag{17}$$

where P_{abs} is the absorption power per unit volume. P_V is the power loss per unit volume via volumetric processes

$$P_V = n_e \sum_j \left(\sum_i n_j \varepsilon_{inel,j}^{(i)} k_{inel,j}^{(i)} + n_j \frac{3m_e}{m_j} T_e k_{el,j} \right), \quad (18)$$

where m_e is the electron mass and n_j is the number density of species j, $k_{inel,j}^{(i)}$ is the rate coefficient of an inelastic process i involving species j, and $\varepsilon_{inel,j}^{(i)}$ is the corresponding threshold energy. $k_{el,j}$ is the rate coefficient for electron elastic scattering on species j. The collisional energy loss per electron-ion pair created is expressed as $\varepsilon_c = \sum_i \varepsilon_{inel,j}^{(i)} k_{inel,j}^{(i)} / k_{iz,j}$ and is shown in Fig. 1 versus electron temperature for H and H_2. $k_{iz,j}$ is the ionization rate coefficients for H and H_2. The collisional energy losses per electron-ion pair created for H atoms and H_2 molecules predicted by both the codes agree very well with each other.

The power loss at the chamber wall per unit volume P_W is given as

$$P_W = \sum_i n_i (\varepsilon_i + \varepsilon_e) u_{B,i} \frac{A_{\text{eff}}}{V}, \quad (19)$$

where $\varepsilon_e = 2T_e$ is the mean kinetic energy per each electron lost, and $\varepsilon_i = V_p + V_s$ is the mean kinetic energy per each ion lost.[44] V_p is the plasma potential,[44] and V_s is the sheath potential.[45]

C. Interactions of neutral species with the surface

The interactions of neutrals with the walls include the wall recombination of ground-state H atoms into molecules, the wall quenching of excited states of H atoms,[26] and the de-excitation of vibrationally excited hydrogen molecules.[48,49] The rate coefficient is given as[50]

$$k_{s,wall} = \left[\frac{\Lambda^2}{D_{eff,s}} + \frac{2V(2-\gamma_s)}{A v_s \gamma_s} \right]^{-1}, \quad (20)$$

where Λ is the effective diffusion length of neutral species[51] and A is the surface area of the chamber wall. γ_s is the wall quenching coefficient. The H atoms undergo collisions with the walls to become H_2 molecules, where the recombination coefficient $\gamma_H = 0.1$ corresponding to the stainless steel walls is adopted in the model.[52] The H (n = 2, 3) atoms undergoing collisions with the walls were assumed to be deexcited to the ground states of H atoms, and the quenching coefficient $\gamma_{H(n)}$ is set to 1 due to the lack of data. The wall deexcitation rate coefficient of vibrational states, i.e., Eq. (20), used in the GEVKM[25,26] caused overestimation of the loss of vibrational states at high pressures. Therefore, it was modified in this work. For the wall loss of vibrational states, $\gamma_s = 1$ has been assumed. It indicates that the $H_2(\upsilon)$ particles are always deexcited in collisions with the walls. The rate coefficient for the repopulation of vibrational states of $H_2(\upsilon)$ molecules flowing from the walls is given as $k_{s,wall} = (\Lambda^2/D_{eff,s} + 2V/Av_s)^{-1} \gamma_{H_2(\upsilon' \to \upsilon)}$. The repopulation coefficients $\gamma_{H_2(\upsilon' \to \upsilon)}$ used in this paper are based on the vibrational distribution of H_2 molecules reflected from the walls.[48,49] υ' is any higher vibrational level than υ. The fixed rate coefficient was implemented in both the GMNHIS and the GEVKM. The effective multicomponent diffusion coefficients according to Blanc's law are given by[53,54]

$$\frac{1}{D_{eff,s}} = \sum_{\substack{p=1 \\ p \neq s}}^{N_s} \frac{1}{D_{ps}} \frac{n_p}{n - n_s}. \quad (21)$$

This diffusion coefficient is different from that in the work of Huh *et al.*[31] where the Knudsen diffusion seems to be double-counted. The second term of Eq. (20) is found to have the same form as Knudsen diffusion when γ_s is equal to 1. The Knudsen diffusion is therefore not included in Eq. (21) again. The binary diffusion coefficient assuming the same temperature of heavy species is given by[54]

$$D_{ps} = \sqrt{\frac{2\pi k_B (m_p + m_s) T_{gas}}{m_p m_s}} \frac{3}{16 n \Omega_{ps}^{(1,1)}}, \quad (22)$$

where the $\Omega_{ps}^{(1,1)} = \pi \sigma_{ps}^2 \Omega_{ps}^{(1,1)^*}$, with a reduced collision integral $\sigma_{ps}^2 \Omega_{ps}^{(1,1)^*}$ that was tabulated in the work of Capitelli *et al.*,[55] and n is the total number density of both neutral species and positive ions. The ion mean free path λ_i mentioned earlier can be obtained from the effective multicomponent diffusion coefficients as

$$\lambda_i = \frac{1}{\sum_{p=1}^{N_i} n_p \Omega_{pi}^{(1,1)}} = \frac{16n}{3\sqrt{\frac{2\pi k_B T_{gas}}{m_i}} \sum_{p=1}^{N_i} \sqrt{1 + \frac{m_i}{m_p}} \frac{n_p}{D_{pi}}}. \quad (23)$$

The diffusion coefficient D_i for positive ions used to calculate the ambipolar diffusion coefficients in Eqs. (6)–(8) has the same expression as Eq. (21).

D. Chemistry mechanism of low pressure H_2 plasma

Table I shows the kinetic reactions considered in the model. It involves electrons, ground-state molecules H_2, atoms H, molecular ions H_3^+ and H_2^+, atomic ions H^+, negative ions H^-, 14 vibrationally excited molecules $H_2(\upsilon = 1 - 14)$, and electronically excited atoms H (n = 2, 3). The reaction set mainly refers to the previous study[28] and is extended based on the benchmarking against GEVKM. Special attention is paid to the vibrational kinetics because it affects the H^- production.

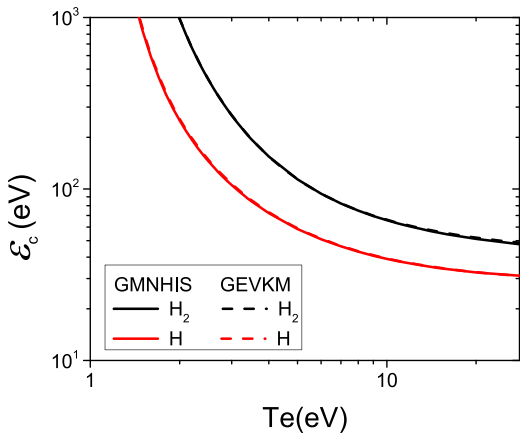

FIG. 1. Collisional energy loss versus electron temperature for H and H_2.

TABLE I. Reaction set considered in the model.

Reaction	Description	References
Volume reactions		
1. $e + H_2 \rightarrow e + H_2$	Elastic scattering	57
2. $e + H \rightarrow e + H$	Elastic scattering	56
3. $e + H_2 \rightarrow 2e + H^+ + H$	Dissociative ionization	58
4. $e + H_2 \rightarrow 2e + H_2^+$	Molecular ionization	57
5. $e + H_2 \rightarrow e + H + H$	Dissociation	57
6. $e + H_2 \rightarrow e + H + H(n = 2, 3)$	Dissociation	58
7. $e + H_2 \rightarrow H^- + H$	Dissociative electron attachment	9
8. $e + H \rightarrow 2e + H^+$	Ionization	9
9. $e + H \rightarrow e + H(n = 2, 3)$	Electronic excitation	58
10. $e + H(n = 2) \rightarrow e + H(n = 3)$	Electronic excitation	58
11. $e + H(n = 2, 3) \rightarrow 2e + H^+$	Ionization	58
12. $e + H_2^+ \rightarrow e + H + H^+$	Dissociative excitation	9
13. $e + H_2^+ \rightarrow e + H(n = 2) + H^+$	Dissociative excitation	58
14. $e + H_2^+ \rightarrow 2H$	Dissociative recombination	59
15. $e + H_3^+ \rightarrow H_2^+ + H^-$	Dissociative recombination	60
16. $e + H_3^+ \rightarrow 2H + H^+ + e$	Dissociative excitation	58
17. $e + H_3^+ \rightarrow 3H$	Dissociative recombination	59
18. $e + H_3^+ \rightarrow H + H_2$	Dissociative recombination	59
19. $e + H^- \rightarrow H + 2e$	Electron detachment: ED	58
20. $H_2^+ + H \rightarrow H^+ + H_2$	Charge exchange	59
21. $H_2^+ + H_2 \rightarrow H_3^+ + H$	H_3^+ ion formation	61
22. $H^+ + H^- \rightarrow 2H$	Mutual neutralization: MN	62
23. $H^+ + H^- \rightarrow H + H(n = 2, 3)$	Mutual neutralization: MN	63
24. $H_2^+ + H^- \rightarrow 3H$	Mutual neutralization: MN	62
25. $H_2^+ + H^- \rightarrow H_2 + H$	Mutual neutralization: MN	63
26. $H_3^+ + H^- \rightarrow 4H$	Mutual neutralization: MN	62
27. $H_3^+ + H^- \rightarrow 2H_2$	Mutual neutralization: MN	63
28. $H^- + H \rightarrow e + H_2$	Associative detachment: AD	63
29. $H(n = 3) \rightarrow H(n = 2) + h\nu$	Radiative decay	64
30. $H(n = 2, 3) + H_2 \rightarrow H_3^+ + e$	Quenching of H(n) by H_2	65
31. $H(n = 2, 3) + H_2 \rightarrow 3H$	Quenching of H(n) by H_2	65
32. $e + H_2(\upsilon) \rightarrow e + H_2(\upsilon')$	Resonant electron-vibration excitation: eV	66 and 67
33. $e + H_2(\upsilon) \rightarrow e + H_2(\upsilon') + h\nu$	Radiative decay and excitation: EV	8
34. $e + H_2(\upsilon) \rightarrow e + H + H$	Dissociation via $b^3\sum_u^+$: D	68
35. $e + H_2(\upsilon) \rightarrow H + H^-$	Dissociative electron attachment: DA	9
36. $H + H_2(\upsilon) \rightarrow H + H_2(\upsilon')$	Vibrational-translational relaxation: Vt	69
37. $H_2(\omega) + H_2(\upsilon) \rightarrow H_2(\omega) + H_2(\upsilon \pm 1)$	Vibrational-translational relaxation: VT	63
38. $H^- + H_2(\upsilon) \rightarrow H_2(\upsilon - 2) + H + e$, $(2 \le \upsilon \le 6)$	Electron detachment in collisions with $H_2(\upsilon)$: EDV	70
39. $e + H_2 \rightarrow e + H_2(b^3\Sigma_u^+, a^3\Sigma_g^+, c^3\Pi_u, B^1\Sigma_u^+, C^1\Pi_u, E, F^1\Sigma_g^+, e^3\Sigma_u^+)$	Electronic excitation	57
Surface reactions		
40. $H_3^+ + \text{wall} \rightarrow H_2 + H$	Ion wall recombination	51
41. $H_2^+ + \text{wall} \rightarrow H_2$	Ion wall recombination	51
42. $H^+ + \text{wall} \rightarrow H$	Ion wall recombination	51
43. $H + H + \text{wall} \rightarrow H_2$	H wall recombination	50 and 52
44. $H\,(n = 2, 3) + \text{wall} \rightarrow H$	H(n) wall recombination	26 and 50
45. $H_2(\upsilon) + \text{wall} \rightarrow H_2(\upsilon')$, $(\upsilon' < \upsilon)$	Vibrational de-excitation: WD	48 and 50

Some important reactions, such as the EV process of the $H_2(\upsilon = 0)$ molecules and the vibrational-translational relaxation in collisions with molecular hydrogen (VT), were omitted in the previous study.[28] The EV process of the $H_2(\upsilon = 0)$ molecules can significantly increase the densities of high-lying vibrational states of H_2 molecules that are the most efficient in the H^- production, due to the higher number density of the $H_2(\upsilon = 0)$ vs. other vibrational states $H_2(\upsilon = 1 - 14)$. The VT collisions can depopulate high vibrational states $H_2(\upsilon = 10 - 14)$, especially at relatively high pressures. The vibrational-translational relaxation in collisions with H atoms (Vt) and the electron detachment in collisions with vibrationally excited hydrogen molecules (EDV) are also included in GMNHIS, due to their roles played at high pressures. The importance of the $H_2(\upsilon)$ wall relaxation has been stressed by Hiskes and Karo.[48] The assumption of $H_2(\upsilon)$ molecules de-exciting only to the adjacent lower state, used in the previous paper,[28] has been replaced by de-excitation to any of the lower states, same as in GEVKM. The wall quenching coefficients of $H_2(\upsilon)$ molecules $\gamma_{H_2(\upsilon' \rightarrow \upsilon)}$ are discussed in conjunction with Eq. (20). GMNHIS also includes various electronic excitations of hydrogen molecules (reaction 41). Due to low number

densities of excited states, they are not explicitly tracked in the particle balance equations, but are added to account for energy losses in the power balance. The cross sections used here are adopted from the recently published studies.[8,9,26,48,50–52,56–70]

III. CODE BENCHMARKING OF GMNHIS AGAINST GEVKM FOR RF DISCHARGE

Code benchmarking of GMNHIS against GEVKM[25,26] is implemented for a cylindrical RF discharge.[38] The source chamber is a quartz tube with a diameter of 12 cm and a height of 14 cm. The absorption power is 1000 W, and the gas pressure varies from 1 to 30 Pa. Some differences between the two codes must be clarified. First, the number density of H_2 molecules in the GEVKM is calculated using the particle balance equation with accounting for pumping of feedstock gas in and out of the discharge chamber. In the GMNHIS, the equation of state is implemented to obtain the number density of H_2 molecules from specified discharge pressure and gas temperature. The effect of this difference on the plasma parameters is found to be negligible in the investigated discharge parameters range. Second, even if the sets of volume reactions considered are not exactly the same, the reactions significantly affecting the plasma parameters are the same between these two models. Additional heavy-particle collisions included in the GEVKM[26] that are important at high discharge pressures are excluded in the GMNHIS due to the relatively low pressures considered in this study. Last but not least, two codes used different approximation methods for reaction rate coefficients. The lookup table was used in the GMNHIS, while fitting was used in the GEVKM.

A. H^- number density and n_{H^-}/n_e ratio as functions of pressure

H^- number density and n_{H^-}/n_e ratio obtained in simulations with two codes are shown, vs. pressure, respectively, in Figs. 2(a) and 2(b). As for H^- number density, the two codes are in good qualitative and quantitative agreement in the investigated pressure range, except for the slight difference at relatively high pressures where GMNHIS predicts a slightly higher value. The H^- number density first increases and then decreases with increasing pressure. Figure 2(b) shows n_{H^-}/n_e ratio as a function of pressure, and a good agreement is achieved between the two models. In order to understand the small discrepancy in the H^- number density at higher pressures, the electron properties as well as other parameters responsible for production and destruction of H^- are investigated below.

B. Electron temperature and electron number density as functions of pressure

In Figs. 3(a) and 3(b), the electron temperature and electron number density are shown vs. pressure, respectively. Excellent agreement in electron temperature is achieved between the codes in the investigated pressure range except for 1 Pa. Both codes predict the electron temperature to decrease with increasing pressure, because a higher rate of elastic and inelastic collisions results in increased electron energy loss. Very good agreement in electron number density obtained by two codes is due to almost the same collisional energy loss for H and H_2 shown in Fig. 1. In addition to electrons, $H_2(v)$ molecules are the other reactants in the DA processes responsible for H^- production, and the comparison of the VDFs predicted by the two models is presented in what follows.

C. VDFs at two different pressures

Figure 4 shows the VDF at two pressures: 1 Pa and 10 Pa. The density values predicted by the two codes are in very good qualitative agreement in both cases. Both codes show that the VDF is non-Boltzmann, characterized by a plateau at the intermediate vibrational levels, and the higher pressure leads to a significant decrease in the density of very high vibrational states due to the VT processes. The slightly higher VDF predicted by the GMNHIS than that in the GEVKM is possibly due to the inclusion of additional processes destroying $H_2(v)$ into the GEVKM that are mainly important at high pressures. Therefore, the higher H^- number density predicted by GNNHIS is mainly due to a slightly higher VDF, regarding almost the same electron number densities and electron temperatures predicted by the two codes.

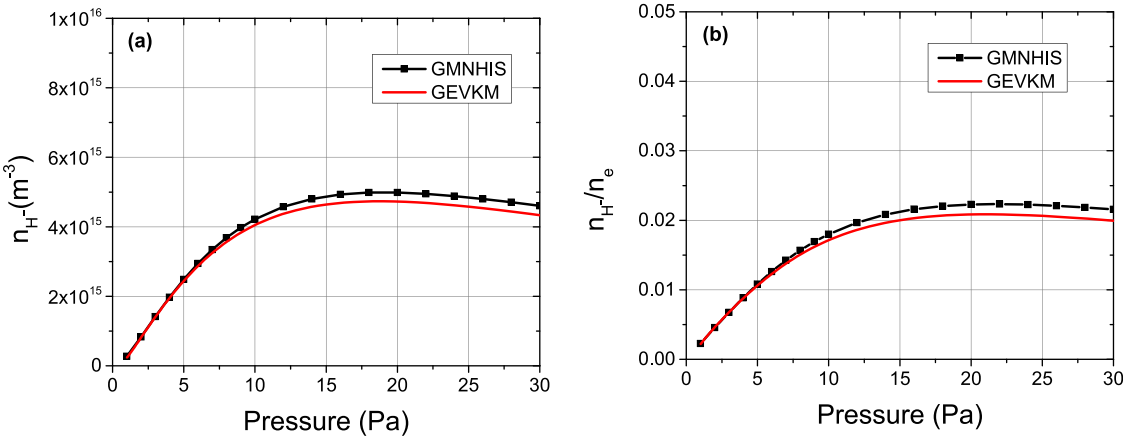

FIG. 2. H^- number density (a) and n_{H^-}/n_e ratio (b) as functions of pressure.

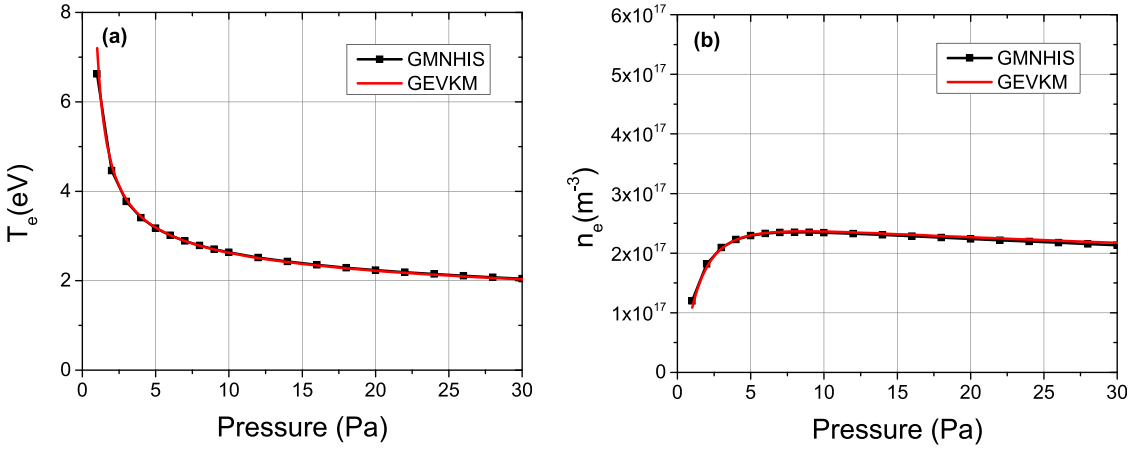

FIG. 3. Electron temperature (a) and electron number density (b) as functions of pressure.

D. Positive ion number density and H(n = 1–3) atom number density as functions of pressure

Figure 5 shows the number densities of three positive-ion species as functions of pressure. The two codes are in very good qualitative agreement. The densities of H_3^+ and H_2^+ predicted by two codes achieve very good quantitative agreement. As the pressure increases, H_2^+ number density decreases, H^+ number density first slightly increases and then decreases, and H_3^+ number density first increases and then gradually decreases. The variation in the H_3^+ number density versus pressure is very similar to that of electron number density, since H_3^+ is the prevailing ion species. The slightly higher H^+ number density at higher pressures obtained with GMNHIS is possibly due to the lack of the charge exchange reaction between H^+ and $H_2(v)$ that was included into the GEVKM . In this work, the most important reaction producing the H_3^+ is the collision between $H(n = 2)$ and H_2, i.e., reaction 30 in Table I. The number densities of electronically excited H atoms and the ground-state H atoms vs. pressure are shown in Figs. 6(a) and 6(b), respectively. The number densities of $H(n = 2, 3)$ predicted by GMNHIS agree very well with those calculated by GEVKM, and thus, the H_3^+ number densities predicted by both codes are found to be in good agreement. The $H(n = 2)$ atoms are mainly produced by the electronic excitation of H atoms at pressures above 2 Pa. The good agreement of H atom number density predicted by both codes achieves almost the same $H(n = 2)$ density.

IV. VALIDATION OF GMNHIS WITH EXPERIMENTS FOR ECR DISCHARGE

Validation of the GMNHIS code outlined in Sec. II has been performed for an ECR discharge. All the experimental results are obtained in the negative ion source "Prometheus I."[21–23] In Fig. 7, a conceptual diagram of the source is presented. It consists of a cubic (24 cm inner edge) stainless steel chamber with viewports for diagnostic installation. The plasma is sustained by a 2D network of ECR plasma elementary sources and the present measurements are realized 6.5 cm below the middle-plane of the magnets, as depicted in the left part of Fig. 7. The region between magnets and 6.5 cm below the middle-plane of the magnets is defined as the upper part. The region below the upper part is the lower part of the chamber. Each elementary source is driven by an independent microwave solid-state power supply (2.45 GHz;

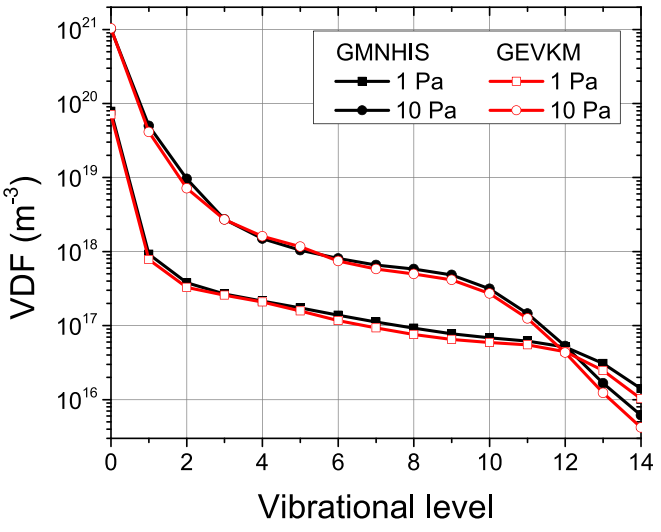

FIG. 4. Predicted vibrational distributions of H_2 molecules at 1 Pa and at 10 Pa.

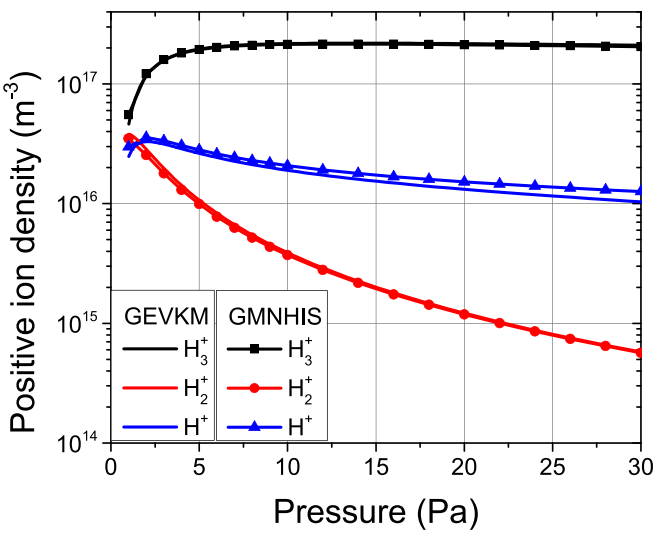

FIG. 5. Positive ion number density as a function of pressure.

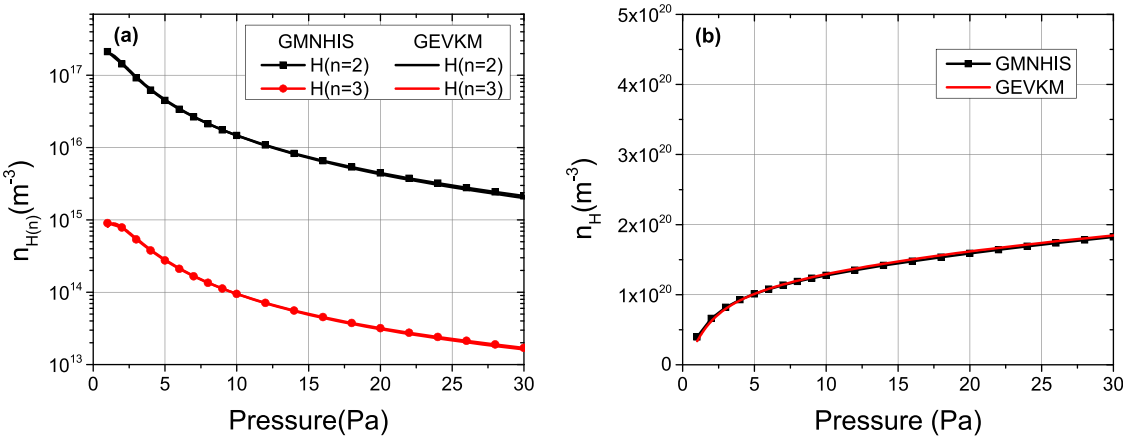

FIG. 6. Number densities of electronically excited H atoms (a) and of ground-state H atoms (b) as functions of pressure.

180 W). A tuner embedded on the main body of each source is used for impedance matching which maximizes the microwave power absorbed by the plasma. The impedance matching is manually optimized in order to reduce microwave power reflection (maximum accepted reflection <3%). The elementary sources and their power supplies are cooled by water circulation (CoolMaster K-003.6). A turbo-molecular pump adapted under the bottom flange evacuates the source down to 1.3332×10^{-5} Pa (in Refs. 21 and 23 the base pressure was 4×10^{-4} Pa due to the Vacuum Ultra-Violet (VUV) diagnostic tools installed on the source). Pure H_2 (N50) is introduced by a digital mass flow controller (MKS 1179B) at a flow rate between 2.1 and 23.2 sccm. The working pressure varies respectively between 0.13332 and 2.6664 Pa (filling gas pressure) and it is accurately monitored with an absolute pressure transducer (MKS Baratron 627D).

Each ECR elementary source consists of two parts: a cylindrical samarium-cobalt (Sm_2Co_{17}) permanent magnet, magnetized along its axis, and a coaxial line parallel to the magnetization vector, having an open end at the rear pole of the magnet. The microwave power can thus be transmitted through the plasma and be mostly absorbed near the region where the ECR condition is fulfilled. For the microwave frequency of 2.45 GHz, the required magnetic field is 875 G. Clearly, the plasma produced below the middle-plane of the ECR zones is different with respect the one produced over the middle-plane, due to the presence of the grounded microwave guides, the top flange etc. In any case, the main source volume is below the ECR zones and the input power is considered in GMNHIS to be uniformly absorbed by the plasma volume defined by the dashed line in Fig. 7 (left part). The plasma is further considered to freely diffuse downstream of

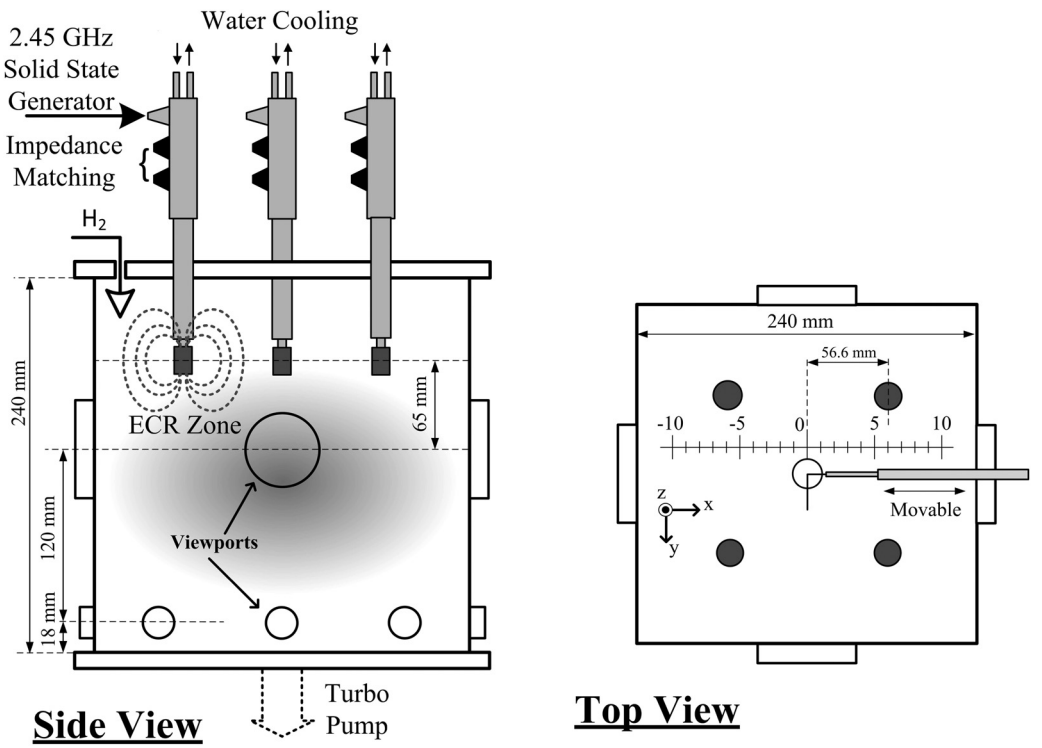

FIG. 7. Side view (left) and top view (right) of the experimental setup of the ECR source.[23]

this volume where no ionization is assumed. A perfect open-boundary condition discussed in conjunction with Eq. (5) is imposed in GMNHIS for predicting the plasma parameters in the above-defined plasma volume. The number densities of different species obtained with GMNHIS are spatially integrated in this volume. The absorption of the power is fixed at 900 W.

A cylindrical tungsten electrostatic probe is immersed in the plasma as presented in Fig. 7 (right). The probe is made from a 0.25 mm in diameter tungsten wire and the tip (exposed to the plasma) is L-bent in order to be aligned with the laser beam for the photo-detachment measurements. The tip is 15 mm in total length with the bent part being 11 mm. The rest of the wire is housed in a telescopic configuration of dielectrics (alumina tube inside a wider quartz tube). The quartz tube is supported inside a stainless steel tube that ends in a standard BNC vacuum feed-through. A CF flange-to-quick connect coupling adapter makes a vacuum joint with the steel tube and at the same time allows the linear translation of the probe.

The acquisition of electrostatic probe current-voltage (I-V) curves is accomplished with a custom-made system.[71] Each measurement procedure includes 10 s of probe cleaning by electron current-induced incandescence followed by another 10 s of cooling-down. The acquisition is realized point by point in steps of approximately 100 mV. For each point, 2^{12}–2^{13} voltage-current samples are averaged in order to reduce plasma-induced noise.

At the probe position, the magnetic field of the ECR modules has a vertical downward direction and a magnitude of 51 G, while the probe tip itself is oriented horizontally (i.e., perpendicular to the magnetic field). The lowest electron temperature observed during the present experiments is about 0.5 eV which corresponds to an electron Larmor radius of about 0.34 mm. Thus, even in the worst case, the probe radius (0.125 mm) is sufficiently smaller than the electron Larmor radius, validating the use of the classical non-magnetized probe theory.

Typical plasma parameters, i.e., floating and plasma potential, electron densities, and temperatures, are obtained from numerical treatment and fitting procedures on the I-V curve data. More specifically, plasma potential is estimated as the maximum of the I-V curve first derivative and positive ion current is linearly extrapolated from high retarding potentials and subtracted from the I-V curve. The remaining current (electron current) is fitted as the sum of two exponentials, which corresponds to a bi-Maxwellian EEDF. The experimental EEDF is derived from the second derivative of the probe total current (Druyvesteyn method).

The photo-detachment diagnostic technique with one laser beam is used for the determination of the negative ion absolute density. A short (∼5 ns) Nd:YAG 1064 nm laser pulse, generated from a Quantel Brilliant EaZy (330 mJ/pulse) unit, is concentrically aligned with the bent part of the probe tip and detaches the extra electron of negative ions inside the irradiated cylindrical volume. The excess (i.e., photo-detached) electrons, in the section of the irradiated volume that contains the bent part of the probe tip, sharply increase the electron current collected by the positively biased probe. The density of negative ions can then be calculated from the amplitude of the current pulse. To avoid any potential errors that arise from the use of the traditional capacitive decoupling circuit, a wideband current transformer (Pearson electronics 6585; 400 Hz–200 MHz), connected directly to a digital oscilloscope (LeCroyWaveSurfer 104Xs-A; 1 GHz/5 GSamples s^{-1}), is used to measure the transient current pulse due to the photo-detached electrons.

Various parameters of the photo-detachment diagnostic technique are properly set for its valid application. First, the laser radius is chosen to be 3 mm which sufficiently exceeds the probe collection radius (∼0.1 mm which is the typical Debye length for the present experimental conditions). Second, the probe bias has been set to +15 V (i.e., 7–8 V above plasma potential) which is sufficient for collecting all the detached electrons without causing the incandescence of the probe tip due to electron current. To establish this, a series of measurements was realized which demonstrated that a +15 V bias leads to the saturation of the photo-detached electron current. Finally, the energy density of the laser beam is chosen to be around 70 mJ cm^{-2} which is high enough to destroy all the negative ions in the irradiated volume. This is ensured by the saturation of the photo-detachment signal, while the latter is being recorded versus the increasing laser power.

A. Electron number density as a function of pressure

Electron number density as a function of pressure is shown in Fig. 8. The experimental data are adopted from Ref. 23. As shown in Fig. 8(a), the electron number density shows first a rapid increase, and then sluggish growth with increasing pressure. This dependence is qualitatively reproduced by GMNHIS. Quantitatively, electron number density predicted by GMNHIS is higher than the experimental values. This discrepancy could be attributed to the fact that the experimental data are provided from local measurements, whereas the model considers volume-averaged values. Furthermore, our assumption for the power deposition in the limited volume defined in Fig. 7 (left) is an overestimation of the power, since a part of the 900 W should definitely be consumed elsewhere in the source. Electrons with higher energy in a smaller volume lead to a higher ionization rate, and therefore, a higher electron number density is predicted by GMNHIS. Figure 8(b) shows the experimental cold and hot electron number densities as functions of pressure. The cold electron number density first increases at pressures below 1.6 Pa and then saturates for higher pressures. The hot electron number density keeps increasing with the pressure.

B. Pressure dependence of VDF

The production rate of H^- ions is very sensitive to the VDF, in addition to electron properties. Figure 9 shows the VDF at different pressures predicted by GMNHIS as (a) the logarithmic plot for all vibrational states ($0 \leq \upsilon \leq 14$) and (b) the linear plot for higher vibrational states ($4 \leq \upsilon \leq 12$). It is clear that the densities of higher vibrational states ($4 \leq \upsilon \leq 11$) almost monotonically increase with increasing

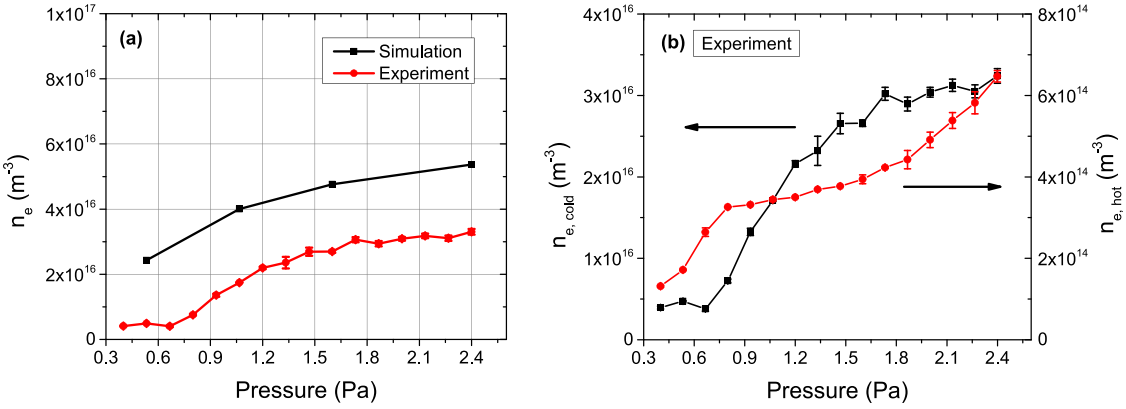

FIG. 8. (a) Electron number density as a function of pressure and (b) cold and hot electron number densities as functions of pressure. The experimental data are taken from Ref. 23.

pressure. The significant relative decrease in $H_2(\upsilon = 12)$ density at high pressure is due to the VT processes.

C. Determination of H^- number density

The number density of H^- ions is estimated by the following formula:

$$n_{H^-} = \frac{\sum_{v=0}^{14} n_{H_2(v)} n_e \langle \sigma_{DA}(\varepsilon), \varepsilon \rangle}{k_{MN} n_+ + k_{AD} n_H + n_e \langle \sigma_{ED}(\varepsilon), \varepsilon \rangle + k_{EDV} n_{H_2(v)}}, \quad (24)$$

where the numerator is the H^- production rate via the DA of electrons to $H_2(\upsilon)$ molecules, while the denominator includes the H^- losses, i.e., mutual neutralization (MN), associative detachment (AD), electron detachment (ED), and electron detachment in collisions with vibrationally excited hydrogen molecules (EDV). The densities appearing on the right hand side of Eq. (24) are obtained using GMNHIS. The rate coefficients involving heavy species (ions and neutrals) are denoted by k, where the coefficients for processes involving electron collisions (DA and ED), i.e., $\langle \sigma_{DA}(\varepsilon), \varepsilon \rangle$ and $\langle \sigma_{ED}(\varepsilon), \varepsilon \rangle$, are related to the corresponding cross section $\sigma(\varepsilon)$ and the EEDF. The experimental EEDFs, approximated as bi-Maxwellians, are adopted from Ref. 23 and are shown in Fig. 10(a). The cross sections for DA of electrons to the selected vibrational states of H_2 molecules are shown in Fig. 10(b).[9] The cross section increases by orders of magnitude with the vibrational quantum number of H_2 molecules varying from 0 to 4. The threshold energy increases with decreasing vibrational quantum number and has a maximum value of 3.72 eV for $\upsilon = 0$. Therefore, at low operating pressures considered here, low energy electrons and high vibrational states of H_2 molecules mainly contribute to the H^- production.

The experimental H^- number density is qualitatively reproduced by the calculation based on Eq. (24) and the comparison is shown in Fig. 11(a). The H^- number density as a function of pressure first increases at pressures below 1.6 Pa and then saturates for higher pressures. Even if the monotonous increase in the $H_2(4 \le \upsilon \le 11)$ densities shown in Fig. 9(b) can promote the production rate of the H^- ions through the DA processes, the saturation of cold electron number density at relatively high pressure (>1.6 Pa) can possibly limit the increase in H^- number density. Figure 11(b) shows the n_{H^-}/n_e ratio as a function of pressure. The simulation qualitatively reproduces the experimental values. The ECR source achieves a high electronegativity (n_{H^-}/n_e) over 10% in the pressure range from 0.53 to 2.4 Pa. This is because the hot electrons are mostly located in the vicinity of the ECR source and do not effectively destroy negative

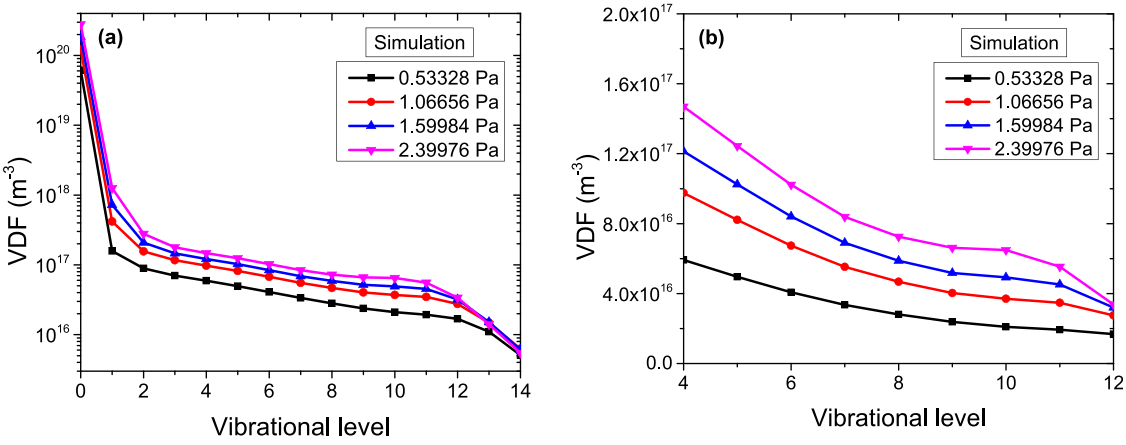

FIG. 9. VDF at different pressures shown as (a) the logarithmic plot for all the vibrational states $(0 \le \upsilon \le 14)$ and (b) the linear plot for higher vibrational states $(4 \le \upsilon \le 12)$.

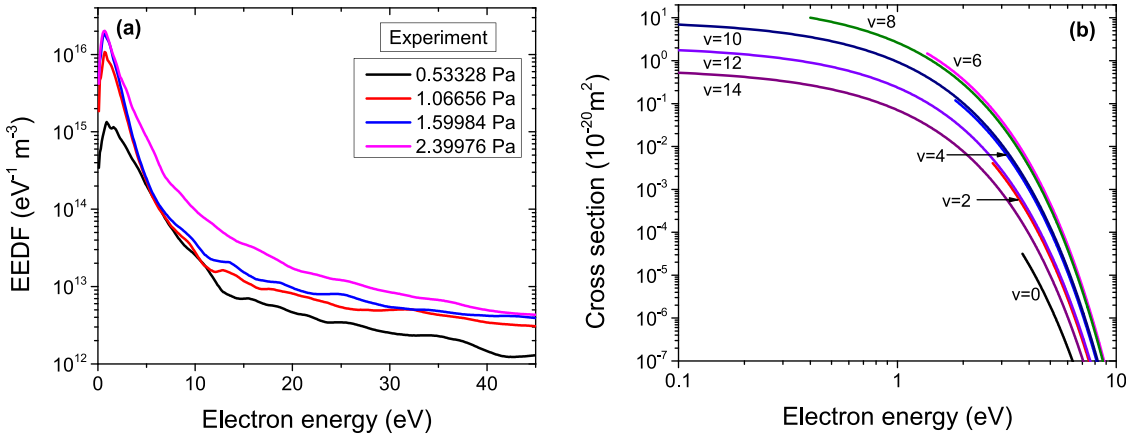

FIG. 10. (a) Experimental EEDF as a function of electron energy at different pressures (Ref. 23) and (b) cross section of DA of electrons to $H_2(\upsilon)$ for selected vibrational states based on the data of Ref. 9.

ions in the lower part of the chamber. The magnetic field in the upper chamber and the sheath at the wall act as filters of hot electrons and only allow the cold electrons to diffuse into the plasma bulk. Similarly, the high n_{H^-}/n_e ratio achieved in the simulation is due to taking into account the experimental EEDF with large population of cold electrons that are responsible for the H^- production. The H^- production would be lower by an order of magnitude if the H^- number density was directly calculated from GMNHIS assuming a single-temperature Maxwellian EEDF. It should also be noted that in this work we have neglected the production of H^- ions due to the DA processes involving the resonant Rydberg electronic state[10] and the recombinative desorption of H atoms from the walls with formation of vibrationally excited hydrogen molecules.[72] These two processes may further increase the predicted H^- number density.

D. H^- creation and loss mechanisms

In order to gain insight into the pressure dependence of H^- number density, we examine the pressure dependence of the reaction rates of creation and loss of H^- ions. These rates are plotted in Fig. 12. The H^- density is calculated from Eq. (24). As mentioned earlier, the H^- ions are mainly produced by the DA of the cold electrons to high vibrational states of H_2 molecules. The vibrational states $H_2(\upsilon = 6-11)$ mainly contribute to the DA processes and therefore to H^- production. The reaction rate of the DA processes increases with increasing pressure. At higher pressures the increase is slower due to the saturation of cold electron density. For the H^- loss mechanisms, the MN processes of H_3^+ and H_2^+ with H^- as well as the AD process of H with H^- are the most important channels. As the pressure increases, the AD process and MN process of H_3^+ with H^- is enhanced due to the increase in number densities of H atoms and H_3^+ ions, respectively. The variation of reaction rates of MN processes with pressure can be understood through presenting the number densities of H_3^+, H_2^+ and H^+ as functions of pressure as shown in Fig. 13. The reaction rates of EDV and ED processes increase with pressure due to the increase in number densities of vibrational states and of hot electrons, but the contributions of these two processes are negligible in the investigated pressure range.

V. CONCLUSION

The Global Model for Negative Hydrogen Ion Source (GMNHIS) numerical code was developed and benchmarked against an independently developed code, Global Enhanced Vibrational Kinetic Model (GEVKM). GMNHIS is based on

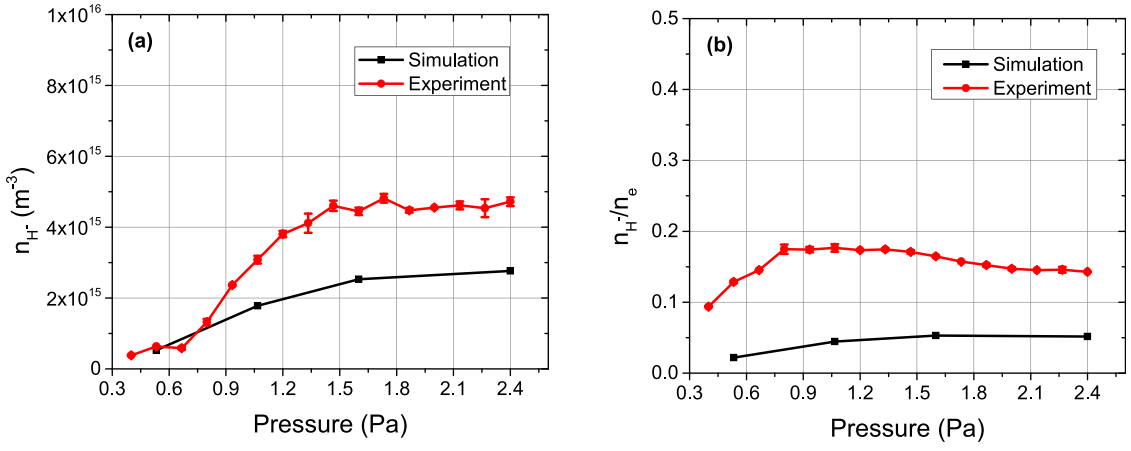

FIG. 11. H^- number density (a) and n_{H^-}/n_e ratio (b) as functions of pressure. The experimental data are taken from Ref. 23.

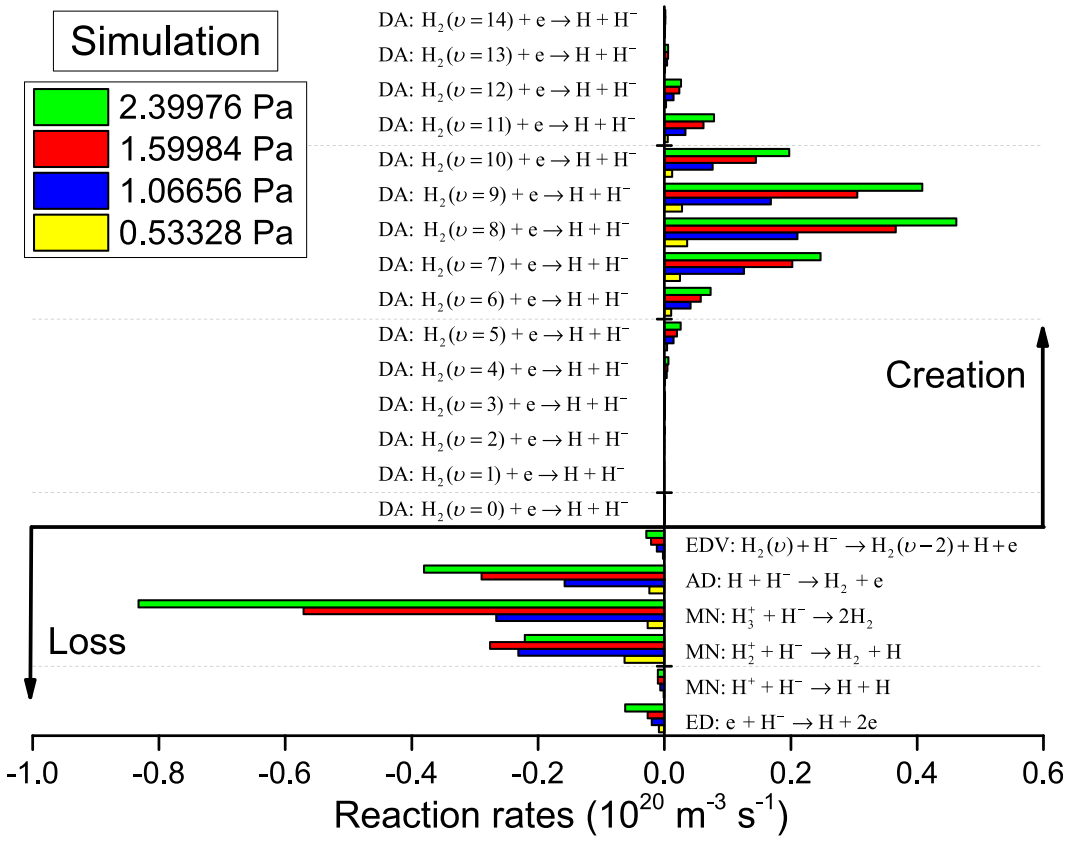

FIG. 12. Reaction rates of the production and loss reactions of H^- ions at different pressures.

the previous work[28] with the extended set of chemical reactions governing vibrational kinetics. Benchmarking has helped us to fix a number of mistakes in both codes and ascertain the chemical reaction data that was used. The initial chemical reaction data were collected separately for both codes and they allowed finding some inconsistency in the published literature. Therefore, the chemical reaction data used in this work are carefully evaluated. Very good agreement has been achieved for pressure dependence of the plasma parameters such as electron temperature, collisional energy loss per electron-ion pair created, electron number density, densities of H_3^+ and H_2^+ ions, and densities of H(n = 1–3) atoms. The very small discrepancies observed in number densities of H^- ions and H^+ ions as well as vibrational distribution function (VDF) are possibly due to the inclusion of additional chemical reactions into the GEVKM that are mostly important at higher discharge pressures. To the authors' knowledge, this is the first study to report a comprehensive benchmarking of two numerical models of Negative Hydrogen Ion Sources (NHIS). Also, GMNHIS has been validated by comparing its predictions with experimental data obtained in measurements in an ECR discharge for H^- production.[23] In the simulations, the H^- production is predicted using GMNHIS and experimentally measured EEDF. We achieve qualitative agreement (and even quantitative agreement for certain conditions) for the H^- number density, which validates the simulations based on the adopted H_2 reaction set and various assumptions used in the numerical model.

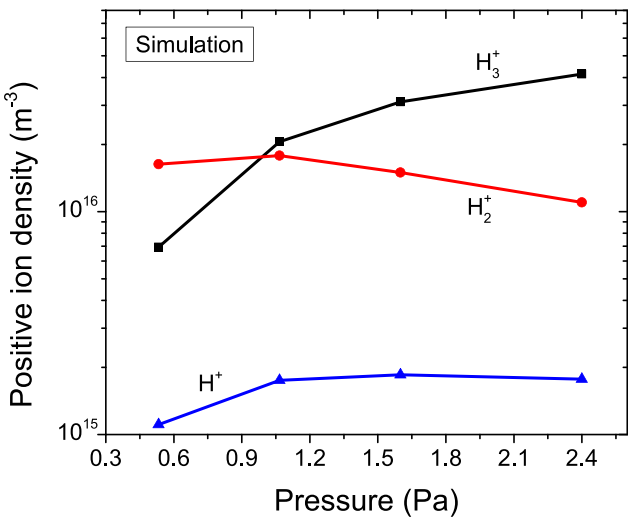

FIG. 13. Positive ion number density as a function of pressure.

Both the experiment and simulation show that the H^- number density first increases and then saturates with increasing pressure. In order to understand the saturation of the H^- production, the pressure dependence of the reaction rates for creation and loss processes of H^- ions has been analyzed. The specific vibrational states $H_2(\upsilon = 6-11)$ mainly contribute to the dissociative attachment (DA) processes and therefore to H^- production. The reaction rates of the DA processes increase with pressure and at higher pressures, the increase is slower due to the saturation of cold electron

density. The mutual neutralization (MN) of H_3^+ with H^- and associative detachment of H with H^- (AD) mainly contribute to the H^- destruction, and the reaction rates of these two processes increase with pressure. Therefore, the saturation of the H^- production at relatively high pressures could be attributed to the saturation of cold electron number density and the enhancement in the MN process of H_3^+ with H^- and the AD process.

The ECR source demonstrates good performance by producing a high n_{H^-}/n_e ratio over 10% in the low-pressure regime. This is because most of the hot electrons are located in the vicinity of the ECR source due to the resonant heating, while cold electrons diffuse to the region away from the sources resulting in increased H^- production. The possible ways to further optimize the H^- production are increasing the cold electron number density by adjusting the size of upper and lower chamber or injecting a high-energy electron beam into the upper chamber, or a low-energy electron beam into the lower chamber in future H^- ion beam sources. In addition, a special chamber wall material with high H atom sticking coefficient can possibly enhance the H^- production by decreasing the loss of H^- ions caused by the AD process. For example, tantalum and tungsten materials with a high H atom sticking coefficient of 0.5 have been proved to be H^- enhancers in the work of Bentounes *et al.*,[73] according to which the production of high vibrational states of H_2 can be significantly increased through the interaction between surface absorbed H atoms with other H atoms.

In the future work, the DA processes involving the resonant Rydberg electronic state and the recombinative desorption of H atoms at the walls with formation of vibrationally excited hydrogen molecules will be included in our models, because these processes can increase the H^- production. Benchmarking and validation studies reported here are essential to using simulation codes as reliable predictive tools, ultimately aiding in developing optimized negative ion beams for ITER and prospective fusion reactors.

ACKNOWLEDGMENTS

This work was supported by the China Scholarship Council (CSC), the National Magnetic Confinement Fusion Science Program, China (Grant No. 2015GB114000), and the National Key R&D Program of China (Grant No. 2017YFE0300106). The work of Igor D. Kaganovich was supported by the U.S. Department of Energy. The authors would like to thank M. Bacal for offering helpful suggestions and R. Celiberto for providing the cross section data for the reactions 32, 33, and 34 in Table I.

[1]E. Speth, H. D. Falter, P. Franzen, U. Fantz, M. Bandyopadhyay, S. Christ, A. Encheva, M. Froschle, D. Holtum, B. Heinemann, W. Kraus, A. Lorenz, Ch. Martens, P. McNeely, S. Obermayer, R. Riedl, R. Suss, A. Tanga, R. Wilhelm, and D. Wunderlich, Nucl. Fusion **46**, S220 (2006).
[2]R. S. Hemsworth and T. Inoue, IEEE Trans. Plasma Sci. **33**, 1799 (2005).
[3]Y. Belchenko, Rev. Sci. Instrum. **64**, 1385 (1993).
[4]R. Hemsworth, H. Decamps, J. Graceffa, B. Schunke, M. Tanaka, M. Dremel, A. Tanga, H. P. L. De Esch, F. Geli, J. Milnes, T. Inoue, D. Marcuzzi, P. Sonato, and P. Zaccaria, Nucl. Fusion **49**, 045006 (2009).
[5]P. Franzen and U. Fantz, Fusion Eng. Des. **89**, 2594 (2014).
[6]M. Allan and S. Wong, Phys. Rev. Lett. **41**, 1791 (1978).
[7]J. M. Wadehra and J. N. Bardsley, Phys. Rev. Lett. **41**, 1795 (1978).
[8]R. Celiberto, R. K. Janev, A. Laricchiuta, M. Capitelli, J. M. Wadehra, and D. E. Atems, At. Data Nucl. Data Tables **77**, 161 (2001).
[9]R. K. Janev, D. Reiter, and U. Samm, *Collision Processes in Low-Temperature Hydrogen Plasma* (Forschungszentrum, Zentralbibliothek, 2003).
[10]R. Celiberto, R. K. Janev, J. M. Wadehra, and J. Tennyson, Chem. Phys. **398**, 206 (2012).
[11]M. Bacal, Nucl. Instrum. Methods Phys. Res. B **37–38**, 28 (1989).
[12]W. Kraus, P. Franzen, B. Heinemann, E. Speth, and O. Vollmer, Fusion Eng. Des. **56–57**, 499 (2001).
[13]P. Franzen, H. Falter, B. Heinemann, Ch. Martens, U. Fantz, M. Berger, S. ChristKoch, M. Fröschle, D. Holtum, W. Kraus, P. McNeely, R. Riedl, R. Süss, S. Obermayer, E. Speth, and D. Wünderlich, Fusion Eng. Des. **82**, 407 (2007).
[14]P. McNeely, S. V. Dudin, S. Christ-Koch, U. Fantz, and NNBI Team, Plasma Sources Sci. Technol. **18**, 014011 (2009).
[15]D. Marcuzzi, P. Agostinetti, M. Dalla Palma, H. D. Falter, B. Heinemann, and R. Riedl, Fusion Eng. Des. **82**, 798 (2007).
[16]D. Marcuzzi, M. Dalla Palma, M. Pavei, B. Heinemann, W. Kraus, and R. Riedl, Fusion Eng. Des. **84**, 1253 (2009).
[17]M. Cavenago, T. Kulevoy, S. Petrenko, G. Serianni, V. Antoni, M. Bigi, F. Fellin, M. Recchia, and P. Veltri, Rev. Sci. Instrum. **83**, 02A707 (2012).
[18]M. Cavenago, G. Serianni, M. De Muri, P. Agostinetti, V. Antoni, C. Baltador, M. Barbisan, L. Baseggio, M. Bigi, V. Cervaro, F. Degli Agostini, E. Fagotti, T. Kulevoy, N. Ippolito, B. Laterza, A. Minarello, M. Maniero, R. Pasqualotto, S. Petrenko, M. Poggi, D. Ravarotto, M. Recchia, E. Sartori, M. Sattin, P. Sonato, F. Taccogna, V. Variale, P. Veltri, B. Zaniol, L. Zanotto, and S. Zucchetti, Rev. Sci. Instrum. **87**, 02B320 (2016).
[19]A. Hatayama, S. Nishioka, K. Nishida, S. Mattei, J. Lettry, K. Miyamoto, T. Shibata, M. Onai, S. Abe, S. Fujita, S. Yamada, and A. Fukano, New J. Phys. **20**, 065001 (2018).
[20]A. A. Ivanov, Jr., C. Rouille, M. Bacal, Y. Arnal, S. Bechu, and J. Pelletier, Rev. Sci. Instrum. **75**, 1750 (2004).
[21]S. Aleiferis, O. Tarvainen, P. Svarnas, M. Bacal, and S. Bechu, J. Phys. D: Appl. Phys. **49**, 095203 (2016).
[22]S. Aleiferis, P. Svarnas, I. Tsiroudis, S. Béchu, M. Bacal, and A. Lacoste, IEEE Trans. Plasma Sci. **42**, 2828 (2014).
[23]S. Aleiferis, P. Svarnas, S. Bechu, O. Tarvainen, and M. Bacal, Plasma Sources Sci. Technol. **27**, 075015 (2018).
[24]A. Krylov, D. Boilson, U. Fantz, R. S. Hemsworth, O. Provitina, S. Pontremoli, and B. Zaniol, Nucl. Fusion **46**, S324 (2006).
[25]S. N. Averkin, N. A. Gatsonis, and L. Olson, IEEE Trans. Plasma Sci. **45**, 2460 (2017).
[26]S. N. Averkin, N. A. Gatsonis, and L. Olson, IEEE Trans. Plasma Sci. **43**, 1926 (2015).
[27]R. Zorat, J. Goss, D. Boilson, and D. Vender, Plasma Sources Sci. Technol. **9**, 161 (2000).
[28]W. Yang, H. Li, F. Gao, and Y. N. Wang, Phys. Plasmas **23**, 123517 (2016).
[29]F. Gaboriau and J. P. Boeuf, Plasma Sources Sci. Technol. **23**, 065032 (2014).
[30]C. M. Samuell and C. S. Corr, Plasma Sources Sci. Technol. **25**, 015014 (2016).
[31]S. R. Huh, N. K. Kim, B. K. Jung, K. J. Chung, Y. S. Hwang, and G. H. Kim, Phys. Plasmas **22**, 033506 (2015).
[32]W. Yang, H. Li, F. Gao, and Y. N. Wang, Plasma Sources Sci. Technol. **27**, 075006 (2018).
[33]W. L. Oberkampf, M. M. Sindir, and A. T. Conlisk, "AIAA guide for the verification and validation of computational fluid dynamics simulations," AIAA Paper No. G-077-1998, 1998.
[34]M. Surendra, Plasma Sources Sci. Technol. **4**, 56 (1995).
[35]M. M. Turner, A. Derzsi, Z. Donko, D. Eremin, S. Kelly, T. Lafleur, and T. Mussenbrock, Phys. Plasmas **20**, 013507 (2013).
[36]J. Carlsson, A. Khrabrov, I. Kaganovich, T. Sommerer, and D. Keating, Plasma Sources Sci. Technol. **26**, 014003 (2017).
[37]F. Gao, R. Y. Zhang, H. Li, Y. Liu, and Y. N. Wang, Phys. Plasmas **24**, 073508 (2017).
[38]F. Gao, H. Li, W. Yang, J. Liu, Y. R. Zhang, and Y. N. Wang, Phys. Plasmas **25**, 013515 (2018).
[39]I. D. Kaganovich and L. D. Tsendin, IEEE Trans. Plasma Sci. **20**, 86 (1992).
[40]I. D. Kaganovich and L. D. Tsendin, IEEE Trans. Plasma Sci. **20**, 66 (1992).
[41]A. J. Lichtenberg, I. G. Kouznetsov, Y. T. Lee, M. A. Lieberman, I. D. Kaganovich, and L. D. Tsendin, Plasma Sources Sci. Technol. **6**, 437 (1997).

[42]J. T. Gudmundsson, Plasma Sources Sci. Technol. **10**, 76 (2001).
[43]P. Chabert, J. Arancibia Monreal, J. J. Bredin, L. Popelier, and A. Aanesland, Phys. Plasmas **19**, 073512 (2012).
[44]M. A. Lieberman and A. J. Lichtenberg, *Principles of Plasma Discharges and Materials Processing*, 2nd ed. (Wiley-Interscience, New York, 2005).
[45]E. G. Thorsteinsson and J. T. Gudmundsson, Plasma Sources Sci. Technol. **19**, 015001 (2010).
[46]D. D. Monahan and M. M. Turner, Plasma Sources Sci. Technol. **18**, 045024 (2009).
[47]E. G. Thorsteinsson and J. T. Gudmundsson, J. Phys. D: Appl. Phys. **43**, 115201 (2010).
[48]J. R. Hiskes and A. M. Karo, Appl. Phys. Lett. **54**, 508 (1989).
[49]F. Taccogna, S. Longo, M. Capitelli, and R. Schneider, IEEE Trans. Plasma Sci. **36**, 1589 (2008).
[50]J. P. Booth and N. Sadeghi, J. Appl. Phys. **70**, 611 (1991).
[51]C. Lee and M. A. Lieberman, J. Vac. Sci. Technol. A **13**, 368 (1995).
[52]C. Gorse, M. Capitelli, M. Bacal, J. Bretagne, and A. Lagana, Chem. Phys. **117**, 177 (1987).
[53]M. Capitelli, C. M. Ferreira, B. F. Gordiets, and A. I. Osipov, *Plasma Kinetics in Atmospheric Gases* (Springer, Berlin, 2000).
[54]R. B. Bird, W. E. Stewart, and E. N. Lightfoot, *Transport Phenomena* (Wiley, New York, 1960).
[55]M. Capitelli, D. Bruno, and A. Laricchiuta, *Fundamental Aspects of Plasma Chemical Physics: Transport*, Springer Series on Atomic, Optical, and Plasma Physics Vol. 74 (Springer, New York, 2013).
[56]G. M. Petrov and J. L. Giuliani, J. Appl. Phys. **90**, 619 (2001).
[57]J. S. Yoon, M. Y. Song, J. M. Han, S. H. Hwang, W. S. Chang, B. Lee, and Y. Itikawa, J. Phys. Chem. Ref. Data **37**, 913 (2008).
[58]R. K. Janev, W. D. Langer, K. Evans, and D. E. Post, *Elementary Processes in Hydrogen–Helium Plasmas: Cross Sections and Reaction Rate Coefficients* (Springer-Verlag, Berlin, 1989).
[59]A. T. Hjartarson, E. G. Thorsteinsson, and J. T. Gudmundsson, Plasma Sources Sci. Technol. **19**, 065008 (2010).
[60]H. Tawara, Y. Itikawa, H. Nishimura, and M. Yoshino, J. Phys. Chem. Ref. Data **19**, 617 (1990).
[61]M. T. Bowers, D. D. Elleman, and J. King, J. Chem. Phys. **50**, 4787 (1969).
[62]M. J. J. Eerden, M. C. M. Van de Sanden, D. K. Otorbaev, and D. C. Schram, Phys. Rev. A **51**, 3362 (1995).
[63]A. A. Matveyev and V. P. Silakov, Plasma Sources Sci. Technol. **4**, 606 (1995).
[64]L. C. Johnson, Astrophys. J. **174**, 227 (1972).
[65]M. Glass-Maujean, Phys. Rev. Lett. **62**, 144 (1989).
[66]M. Capitelli, R. Celiberto, F. Esposito, A. Laricchiuta, K. Hassouni, and S. Longo, Plasma Sources Sci. Technol. **11**, A7 (2002).
[67]R. Celiberto, I. Armenise, M. Cacciatore, M. Capitelli, E. Esposito, P. Gamallo, R. K. Janev, A. Laganà, V. Laporta, A. Laricchiuta, A. Lombardi, M. Rutigliano, R. Sayós, J. Tennyson, and J. M. Wadehra, Plasma Sources Sci. Technol. **25**, 033004 (2016).
[68]R. Celiberto, M. Capitelli, and A. Laricchiuta, Phys. Scr. **T96**, 32 (2002).
[69]B. Gordiets, C. M. Ferreira, M. J. Pinheiro, and A. Ricard, Plasma Sources Sci. Technol. **7**, 363 (1998).
[70]A. V. Dem'yanov, N. A. Dyatko, I. V. Kochetov, A. P. Napartovich, A. F. Pal', V. V. Pichugin, and A. N. Starostin, Sov. J. Plasma Phys. **11**, 210 (1985).
[71]S. Aleiferis and P. Svarnas, Rev. Sci. Instrum. **85**, 123504 (2014).
[72]M. Cacciatore and M. Rutigliano, Plasma Sources Sci. Technol. **18**, 023002 (2009).
[73]J. Bentounes, S. Béchu, F. Biggins, A. Michau, L. Gavilan, J. Menu, L. Bonny, D. Fombaron, A. Bès, Y. A. Lebedev, V. A. Shakhatov, P. Svarnas, T. Hassaine, J. L. Lemaire, and A. Lacoste, Plasma Sources Sci. Technol. **27**, 055015 (2018).